SAND2020-6608J

Optimizing Piezoelectric Material Location and Size for Multiple-Mode Vibration Reduction of Turbomachinery Blades

Christopher R. Kelley
Department of Mechanical and
Aerospace Engineering
University of Central Florida
Orlando, FL 32816
Email: chriskelley9@knights.ucf.edu

Garrett K. Lopp
Experimental Structural
Dynamics Department
Sandia National Labs*
Albuquerque, NM 87185
Email: glopp@sandia.gov

Jeffrey L. Kauffman†
Department of Mechanical and
Aerospace Engineering
University of Central Florida
Orlando, FL 32816
Email: JLKauffman@ucf.edu

Modern turbomachinery blades have extremely low inherent damping, which can lead to high transient vibrations and failure through high-cycle fatigue. Smart materials enable vibration reduction while meeting strict blade requirements such as weight and aerodynamic efficiency. In particular, piezoelectric-based vibration reduction offers the potential to reduce vibration semi-actively while simultaneously harvesting sufficient energy to power the implementation. The placement and size of the piezoelectric material is critical to the vibration reduction capabilities of the system. Furthermore, the implementation should target multiple vibration modes. This work develops a procedure to optimize electromechanical coupling across multiple vibration modes for a representative turbomachinery blade with surface-mounted piezoelectric patches. Experimental validation demonstrates good coupling across three targeted modes with a single piezoelectric patch. Placing the piezoelectric material in regions of high signed strain energy for all targeted modes enables vibration reduction across all of the targeted modes.

1 Introduction

Improvements in manufacturing capabilities have led to the increased use of monolithic blisks, which improve aerodynamic efficiency at the expense of a significant decrease in intrinsic damping. This low damping causes high vibration amplitudes that can lead to high-cycle fatigue and failure of the blisk [1]. Recent research investigates integrated and embedded smart materials, such as piezoelectric materials and shape memory alloys, to reduce turbomachinery blade vibration and extend the lifetime of the blisk [2–13]. The electromechanical coupling of piezoelectric materials enables the tailoring of the structural dynamics of a blade: the mechanical stiffness depends on the electrical boundary conditions. Ideal manipulation of the electrical boundary conditions changes the transmissibility of the structure in a way that reduces vibration.

Piezoelectric-based vibration reduction requires efficient strain transfer from the structure to the piezoelectric material to ensure energy is available for conversion to the electrical domain [7, 8]. Thus, it is critical to place the piezoelectric material in a region of high strain energy to maximize the converted electrical energy [9, 10, 14]. However, the spatial distribution of strain energy depends on the mode shape. Therefore, the optimal placement for one mode may not produce good coupling in another mode. This concept extends to the size of the material, as well. Mechanical impedance matching implies that the optimal material size is different for different modes, even when there is high strain energy in the same location [15]. Since blade vibration reduction methods should target multiple modes, ensuring good coupling across the modes of interest requires optimization of the location and size of the piezoelectric material.

This work develops an assumed modes model of a rep-

---

[*] Sandia National Laboratories is a multi-mission laboratory managed and operated by National Technology & Engineering Solutions of Sandia, LLC, a wholly owned subsidiary of Honeywell International Inc., for the U.S. Department of Energy's National Nuclear Security Administration under contract DE-NA0003525.

[†] Address all correspondence to this author.

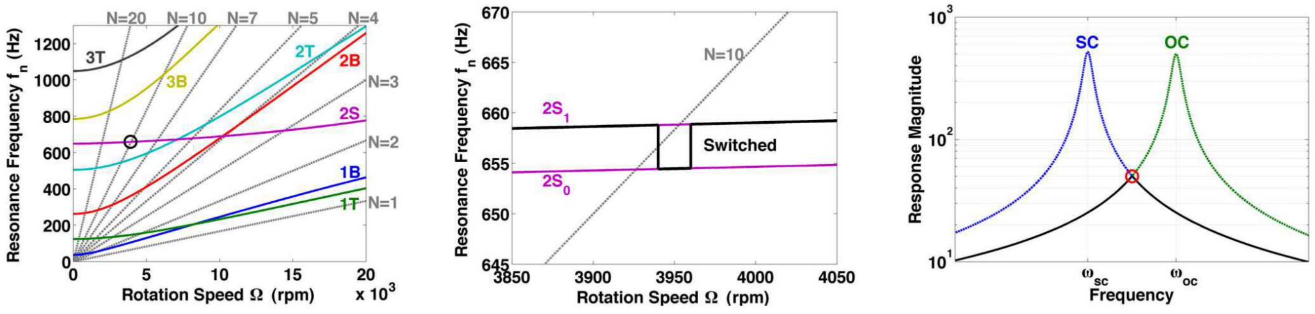

(a) Campbell diagram (b) RFD switching concept (c) RFD vibration reduction

Fig. 1. Resonance frequency detuning switches stiffness states to essentially detune the natural frequency from the excitation frequency

resentative blade to produce stiffness and mass matrices that enable a modal analysis of the system. The model provides analytical calculations of the natural frequencies (which enable calculation of coupling coefficients), mode shapes, and strain energy at each mode. This information provides a measure of the quality of the piezoelectric patch topology for a given mode, enabling optimization of piezoelectric patch location, length, width, and thickness. To investigate optimal blade topology for multiple-mode vibration reduction, this study introduces a cost function that weights the importance of each mode. Minimizing this cost function results in the global optimal placement and size of the piezoelectric material across all modes of interest. Thus, a single piezoelectric patch enables the application of vibration reduction methods across several vibration modes.

2 Background

Piezoelectric material couples mechanical and electrical energy [16]. When integrated into a structure, the piezoelectric material provides a means to manipulate the mechanical state of the structure. The coupling coefficient k characterizes the electromechanical coupling of the structure: the square of the coupling coefficient represents the fraction of energy converted from the mechanical to the electrical domain. The open- and short-circuit natural frequencies (ω_{oc} and ω_{sc}, respectively) provide a convenient calculation of the coupling:

$$k^2 = \frac{\text{electrical energy}}{\text{imposed work}} = \frac{\omega_{oc}^2 - \omega_{sc}^2}{\omega_{oc}^2} \qquad (1)$$

There are three classes of piezoelectric-based vibration reduction: passive, active, and semi-active. Selecting the appropriate class for a given application requires a tradeoff among vibration reduction performance, robustness to unknown and changing parameters, and size requirements. Passive techniques connect the piezoelectric material to a shunt circuit containing only passive circuit elements. The shunt acts as filter that reduces vibration via the electromechanical coupling. While passive techniques can achieve very good vibration reduction, their primary drawback is the need to tune the circuit elements precisely to the targeted frequency [2, 3, 17, 18]. Furthermore, the inductors for the most effective passive shunts are typically very large, preventing passive implementations where size is critical. Proposed circuits for targeting multiple modes require an additional branch for each mode, further increasing the size of passive implementations [19–21]. Active vibration reduction systems apply voltage to the piezoelectric material to create a force that opposes the motion of the structure. Active control provides excellent and robust vibration reduction, but requires a power source [9, 10, 22, 23]. Thus, active methods are not well-suited for applications where it is difficult to include a power source, such as rotating machinery.

Semi-active techniques represent the compromise between passive and active techniques, offering good broadband vibration reduction with extremely low power requirements [4–6, 24–26]. These semi-active techniques are generally insensitive to circuit parameters, enabling the use of small circuit elements. Also, the inherent electromechanical coupling of the piezoelectric material along with the low energy requirements of the system make it possible to harvest enough electrical energy to power the system without an external power source (which is also why the techniques are sometimes called semi-passive) [27]. Thus, semi-active techniques are ideal for turbomachinery applications as they have the potential to meet the strict size requirements and target multiple vibration modes.

Semi-active techniques typically rely on switching the electrical boundary conditions between an open circuit and a shunt circuit, and most of these techniques require four switches per vibration cycle [24–26]. This rapid switching prohibits implementation at high frequencies; in fact, mistimed switches can actually increase vibration levels [28]. However, resonance frequency detuning (RFD) is a semi-active technique designed specifically for turbomachinery blades [4–6]. Turbomachinery spool-up and -down subject blades to high vibrations during each transient passage of resonance. Resonance frequency detuning exploits the change in stiffness between open- and short-circuit states of the piezoelectric material to detune the natural frequency of the structure from the excitation frequency; Fig. 1 demonstrates this concept. The Campbell diagram illustrates resonance frequency crossings during spool-up-down of turbomachinery blades. Zooming in on the RFD switch at the two-

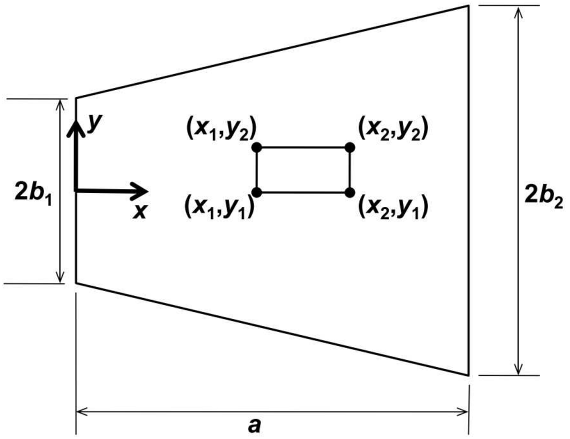

Fig. 2. Representative turbomachinery blade

stripe mode demonstrates the detuning from the resonance frequency that reduces transient vibrations. Switching states at the correct time essentially avoids the resonance crossing and reduces transient vibrations. Significantly, RFD only requires two switching events *per resonance crossing* compared to the typical four switches *per vibration cycle*. Thus, RFD reduces the number of switching events by several orders of magnitude, significantly improving the feasibility of on-blade implementation.

Resonance frequency detuning offers the potential to reduce transient vibrations for any resonance crossing, but only if the piezoelectric material has appreciable coupling for each vibration mode. Since the energy conversion depends on the transfer of strain energy to the piezoelectric material, the placement and size of the piezoelectric material influence the electromechanical coupling at each mode. Previous research optimizes the topology of unimorph and bimorph cantilever beams to maximize coupling in each mode and finds that each mode has different optimal piezoelectric sizes and locations [15]. Various optimization approaches for piezoelectric placement on thin plates draw conclusions for optimal placement for certain modes, but not optimization for vibration reduction of multiple modes [29–33].

For turbomachinery blades, it is especially important to achieve good coupling while limiting the amount of piezoelectric material due to the high stress and rotation of the blade. Thus, it is necessary to optimize topology for all targeted modes simultaneously. This paper targets optimal location and size of piezoelectric material in turbomachinery blades for maximizing electromechanical coupling across multiple modes, extending recent work towards topology optimization [34].

3 Representative Blade Model

This paper models a representative turbomachinery blade to investigate multiple-mode coupling optimization. Figure 2 illustrates the representative trapezoidal plate with a surface-mounted piezoelectric patch. The selected geometry represents typical (untwisted) fan blade geometry since piezoelectric-based vibration reduction primarily targets fan blades. The representative blade is a flat plate to enable analytical calculations; recent research also explores coupling with twisted blades [8]. The plate is cantilevered at $x = 0$ and has span (length) a. The half-chord (half-width) of the plate $b(x)$ varies linearly from b_1 at $x = 0$ to b_2 at $x = a$. The plate is isotropic with uniform thickness h, Young's modulus E, and Poisson's ratio ν. Figure 2 only illustrates one piezoelectric patch, but the model admits multiple patches (in general, the blade has P piezoelectric patches). The patches are assumed to be rectangular such that the coordinates x_{1p}, x_{2p}, y_{1p}, and y_{2p} along with the patch thickness h_p fully define the topology of the p^{th} piezoelectric patch. Each piezoelectric section has Young's modulus E_p, Poisson's ratio ν_p, dielectric permittivity at constant strain ε_p, and equivalent thin-plate piezoelectric constant e_{31p} [35]. Ensuing analyses restrict patch orientation to be aligned with the xy-axes; however, the model and optimization approach also works with rotated patches, but with more computational cost due to nonlinear constraints.

3.1 Assumed Modes Method

The assumed modes method provides analytical approximations of the system matrices, which enable calculation of natural frequencies, mode shapes, and strain energy. As indicated by Eqn. (1), the natural frequencies enable calculation of the electromechanical coupling at each mode—the key parameter for semi-active vibration reduction. Appendix A contains details about the assumed modes formulation, energy terms that lead to the system matrices, and the longer integrals and constants that comprise the system matrices. The subscripts for the following matrix calculations refer to the row and column element of that matrix (e.g., $[K]_{mn}$ is the m^{th} row and n^{th} column of the $[K]$ matrix). Equation (23) relates r and s to m and, in an analogous fashion, u and v to n.

3.2 Stiffness Matrix

Analysis of the strain energy produces the bending stiffness matrix, which is split into the contribution from the plate $[K_o]$ and the contribution from the piezoelectric patches $[K_p]$. The stiffness from the plate is:

$$[K_o]_{rsuv} = \frac{Eh^3}{12(1-\nu^2)}(I_1+I_2+I_3+I_4+I_5) \tag{2}$$

where Appendix A includes the integrals I_1 through I_5, which have the form:

$$I_i = C_i \int_0^a x^{n_1}\left(b_1 + \frac{b_2-b_1}{a}x\right)^{n_2} \mathrm{d}x \tag{3}$$

The integration over x may be carried out analytically in MATLAB using polynomial functions. Now, integrating over the piezoelectric material volume produces:

$$[K_p]_{rsuv} = \sum_{p=1}^{P} \frac{E_p}{12(1-\nu_p)^2}(3h^2h_p + 6hh_p^2 + 4h_p^3) \times (I_{1p} + I_{2p} + I_{3p} + I_{4p} + I_{5p}) \tag{4}$$

The total bending stiffness matrix from the strain energy is the summation of the plate and piezoelectric patch matrices:

$$[K] = [K_o] + [K_p] \tag{5}$$

In addition to these terms, the stiffness matrix must also incorporate the stiffening associated with in-planes loads induced by centrifugal loading. That process follows a similar approach as shown above and is omitted here for brevity; a full derivation can be found in Ref. [8].

3.3 Electrical and Coupling Stiffness Matrices

Analysis of electrical energy and coupled energy leads to electrical and coupled stiffness matrices. The electrical stiffness matrix is diagonal; the P entries are the equivalent capacitances of the piezoelectric patches:

$$[K_e]_{pp} = \frac{\varepsilon_p A_p}{h_p} \tag{6}$$

The coupled energy produces the coupled stiffness matrix:

$$[K_c]_{prs} = \sum_{p=1}^{P} e_{31p}\frac{h+h_p}{2}\left(\frac{r+1}{s}\frac{(x_{2p}^r - x_{1p}^r)(y_{2p}^s - y_{1p}^s)}{a^{r+1}b_2^{s-1}} + \frac{s-1}{r+2}\frac{(x_{2p}^{r+2} - x_{1p}^{r+2})(y_{2p}^{s-2} - y_{1p}^{s-2})}{a^{r+1}b_2^{s-1}}\right) \tag{7}$$

Note the second term in $[K_c]_{prs}$ is equal to zero when $s \leq 2$.

3.4 Mass Matrix

Analysis of the kinetic energy produces the mass matrix. Similar to the bending stiffness, the mass matrix includes plate and piezoelectric patch components. The plate contribution to the mass matrix is:

$$[M_o]_{rsuv} = \frac{2\rho h}{(s+v-1)a^{r+u+2}b_2^{s+v-2}} I_M \tag{8}$$

$$I_M = \begin{cases} \int_0^a x^{r+u+2}(b_1 + \frac{b_2-b_1}{a}x)^{s+v-1}\mathrm{d}x & \text{for } s+v \text{ even} \\ 0 & \text{for } s+v \text{ odd} \end{cases} \tag{9}$$

The piezoelectric contribution to the mass matrix is:

$$[M_p]_{rsuv} = \sum_{p=1}^{P} C_{Mp}(x_{2p}^{r+u+3} - x_{1p}^{r+u+3})(y_{2p}^{s+v-1} - y_{1p}^{s+v-1}) \tag{10}$$

$$C_{Mp} = \frac{\rho_p h_p}{(r+u+3)(s+v-1)a^{r+u+2}b_2^{s+v-2}} \tag{11}$$

Summation of these components produces the mass matrix:

$$[M] = [M_o] + [M_p] \tag{12}$$

3.5 Equations of Motion

The energy formulations enable calculation of the equations of motion via Lagrange's equation:

$$\frac{\mathrm{d}}{\mathrm{d}t}\left(\frac{\partial T}{\partial\{\dot{q}\}}\right) + \frac{\partial(U_{\text{strain}} + U_{\text{elec}} + U_{\text{coupled}})}{\partial\{q\}} = \frac{\partial\delta W}{\partial\{\delta q\}} \tag{13}$$

Here, δW is the virtual work performed by generalized mechanical and electrical external forces (F_m and F_e, respectively). Inserting energy terms, solving, and adding a damping matrix $[C]$ results in the equations of motion:

$$\begin{bmatrix} M & 0 \\ 0 & 0 \end{bmatrix}\begin{Bmatrix} \ddot{q}_m \\ \ddot{q}_e \end{Bmatrix} + \begin{bmatrix} C & 0 \\ 0 & 0 \end{bmatrix}\begin{Bmatrix} \dot{q}_m \\ \dot{q}_e \end{Bmatrix} + \begin{bmatrix} K & -K_c^t \\ K_c & K_e \end{bmatrix}\begin{Bmatrix} q_m \\ q_e \end{Bmatrix} = \begin{Bmatrix} F_m \\ F_e \end{Bmatrix} \tag{14}$$

where inserting electrical boundary conditions produces a non-singular mass matrix.

3.6 Modal Coupling

The effective stiffness matrix depends on the electrical boundary conditions. In the short-circuit case, the voltage is zero ($q_e = 0$) and there is no electromechanical coupling:

$$[K_{\text{sc}}] = [K] \tag{15}$$

For the open-circuit case, the electrical charge is zero ($F_e = 0$), which allows the generalized electrical coordinate to be solved in terms of the generalized mechanical coordinate. Then the effective stiffness matrix becomes:

$$[K_{\text{oc}}] = [K] + [K_c]^t[K_e]^{-1}[K_c] \tag{16}$$

Solving the eigenvalue problem produces the natural frequencies of the structure, which also yields the coupling coefficients via Eqn. (1).

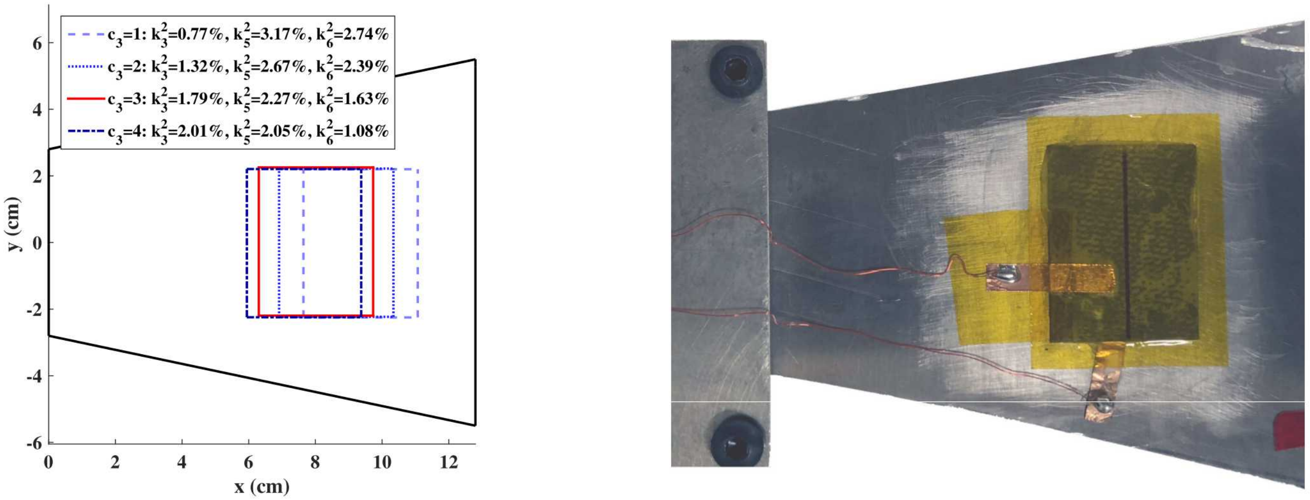

(a) Model

(b) Experiment

Fig. 3. Experimental testing of blade validates analytical model prediction

Table 1. Parameters used in experimental setup

	a (mm)	b_1 (mm)	b_2 (mm)	h (mm)	E (GPa)	ν	ρ (kg/m^2)	ε_{rel}	e_{31} (C/m^2)
Plate	128	28	55	2.03	68.9	0.31	2750	-	-
Piezo	34.3	44.5	44.5	0.267	59.8	0.31	7500	1953	-23.4

Table 2. Comparison of model and experimental coupling

	f_{sc3} (Hz)	k_3^2 (%)	f_{sc5} (Hz)	k_5^2 (%)	f_{sc6} (Hz)	k_6^2 (%)	f_{sc8} (Hz)	k_8^2 (%)
Model	607	1.79	1242	2.27	1788	1.63	2553	3.91
Experiment	549	1.15	1223	1.51	1608	1.45	2458	3.02

4 Optimization

The ability to calculate coupling values analytically provides a rapid estimation of the quality of the piezoelectric material placement and size. This quick computation enables the use of optimization algorithms that minimize a cost function. While more complex geometries prohibit analytical calculations, analysis of low-order geometry provides insight into optimization of more complex geometries. The free parameters for optimization can include any combination of patch location (x_{1p} and y_{1p}), planar size ($L_{xp} \equiv x_{2p} - x_{1p}$ and $L_{yp} \equiv y_{2p} - y_{1p}$), and thickness ($h_p$). Due to the size restrictions for turbomachinery applications, the optimization places constraints on the allowable patch thickness and total piezoelectric material volume. Experimental blade optimization validates the approach.

4.1 Cost Function

Since the goal is to maximize coupling across several modes of interest, this paper proposes a cost function J that is the weighted sum of the square of the coupling coefficients of the modes of interest:

$$J = -(c_1 k_1^2 + c_2 k_2^2 + \ldots + c_N k_N^2) \qquad (17)$$

In this case, minimizing J optimizes coupling from mode 1 to mode N. However, it is not necessary to include all modes in the cost function. For example, a given application might not require vibration reduction in the second mode, so the second term of J would be removed to optimize the modes of interest (equivalent to setting $c_2 = 0$). Also, the weights enable tuning of the cost function to produce the desired coupling distribution. For example, higher weight may be placed on the third mode if it is more important to have good coupling in that mode. Furthermore, a certain weight may be lowered if the optimization is favoring that mode too much at the expense of coupling in other modes. Tuning modal coupling tunes the vibration reduction at each mode, enabling design that maximizes the lifetime of the blade.

4.2 Experimental Validation

This study optimizes the patch location for given dimensions of a pre-cut piezoelectric patch to demonstrate the effect of optimization weights and validate the blade model. Table 1 presents the parameters of the experimental plate and piezoelectric patch. Note the analytical investigation in the following section uses the same plate parameters and piezoelectric material parameters. The optimization considers coupling in modes 3, 5, and 6 (second bending, two-stripe, and third bending, respectively), with varying optimization weights for mode 3 to tune the performance. Figure 3(a) illustrates the optimal piezoelectric material placement using the analytical model while adjusting c_3. Tuning c_3 results in a relatively even coupling distribution in the targeted modes. Thus, a single piezoelectric patch enables vibration reduction in three vibration modes.

This paper compares the blade model to experimental results for the case in Fig. 3(a) with the optimization weights $c_3 = 3$, $c_5 = 1$, and $c_6 = 1$. This case corresponds to piezoelectric patch location $x_1 = 63$ mm and $y_1 = -22$ mm; Fig. 3(b) shows the experimental blade setup. A laser vibrometer measured the tip corner velocity response to a hammer test to produce the frequency response function of the system in open- and short-circuit states. Extraction of modal parameters via circle fit enabled calculation of the coupling coefficient for each mode [36]. Table 2 presents the experimental short-circuit natural frequencies and coupling coefficients for each of the targeted modes along with the model predictions. A by product of optimizing modes 3, 5, and 6 is very high coupling in mode 8, so the table also reports results for this mode. The experimental results show good agreement with the model with frequency errors less than ten percent. The model slightly overestimates stiffness, which may be due to imperfect clamping of the blade [7]. The model also slightly overpredicts coupling, which is expected since the model does not consider the effects of the bond layer and imperfect clamping can also reduce coupling. Overall, the analytical model provides a very good qualitative estimate of the coupling at a low computational cost, making it ideal for topology optimization.

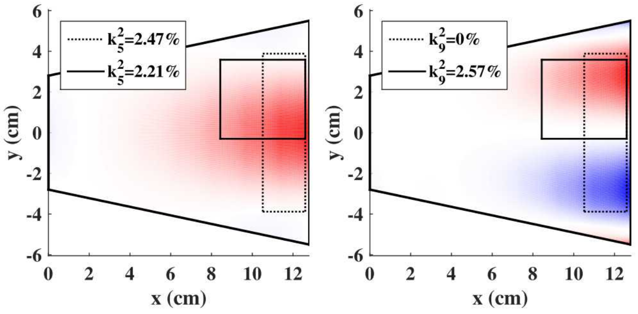

(a) Mode 5 (b) Mode 9

Fig. 4. Effect of signed strain energy distribution (colors) on coupling

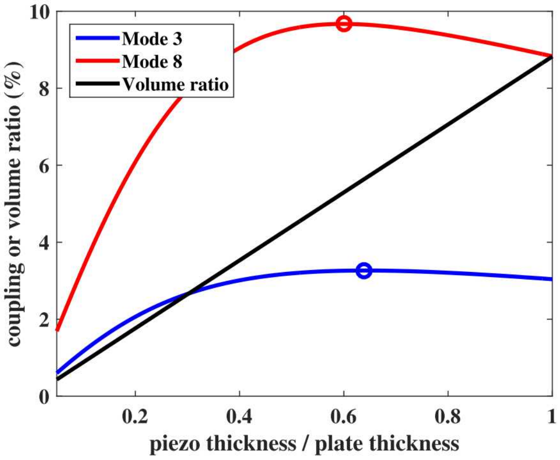

Fig. 5. Effect of patch thickness on coupling

5 Analysis of Optimal Topology

Now this paper uses the analytical blade model to evaluate optimization of piezoelectric material location and size qualitatively for multiple-mode vibration reduction. In particular, this study illustrates the role of signed strain energy in targeting multiple modes with a single piezoelectric patch and demonstrates how to target a wide range of vibration modes with multiple piezoelectric patches.

5.1 Signed Strain Energy

As previously stated, the piezoelectric material needs an efficient transfer of strain energy from the blade to enable vibration reduction, implying that the piezoelectric material should be located in a region of high strain energy. However, it is important to consider whether the strain in the material produces a positive or negative voltage; in other words, is the piezoelectric material subjected to tension, compression, or a combination of the two? One must consider the distribution of the local normal stresses in the piezoelectric patch: a patch located on a nodal line experiences local tension on one side and local compression on the other. Since the patch only has one set of electrodes and tension and compression produce voltages with opposite signs, the magnitude of the piezoelectric voltage is lower than with same-signed normal stress. This concept leads to a new term called the signed strain energy, which includes the sign (tension or compression) in the local strain energy calculation. Thus, the signed strain energy distribution in the blade reflects the distribution of energy available for conversion to the electrical domain. The normal strains and strain energies evaluated at the plate surface as functions of x and y enable calculation of the signed strain energy distribution U_{SSE}:

$$\begin{aligned} U_{\text{SSE}}(x,y) = {} & U_{\text{strain},x}(x,y)\operatorname{sgn}[\varepsilon_{xx}(x,y)] \\ & +U_{\text{strain},y}(x,y)\operatorname{sgn}[\varepsilon_{yy}(x,y)] \end{aligned} \tag{18}$$

Figure 4 demostrates the importance of considering signed strain energy when selecting the location of the piezoelectric material. This example targets vibration reduction in modes 5 and 9 with a single piezoelectric patch (without optimization). Placing the patch to cover large regions of high strain energy (ignoring color in Fig. 4) for both modes results in very good coupling in mode 5. However, even though there is sufficient strain transfer, there is zero coupling in mode 9 because the patch experiences equal amounts of tension and compression. If tension produces a negative potential, compression produces a positive potential. Since the patch only has one set of electrodes, the voltage is exactly

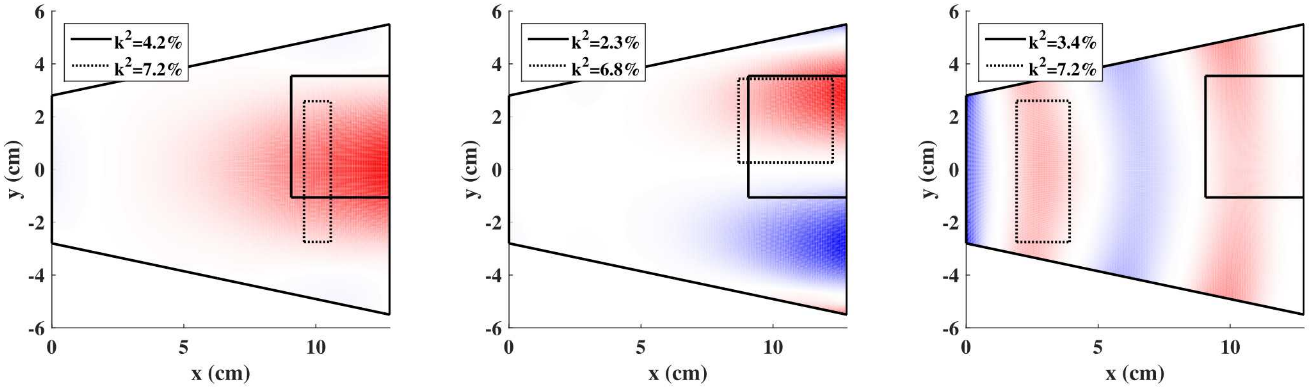

(a) Mode 5 (b) Mode 9 (c) Mode 10

Fig. 6. Simultaneous (solid line) and individual (dotted line) optimization of piezoelectric patch placement and size for modes 5, 9, and 10 (colors show normalized signed strain energy)

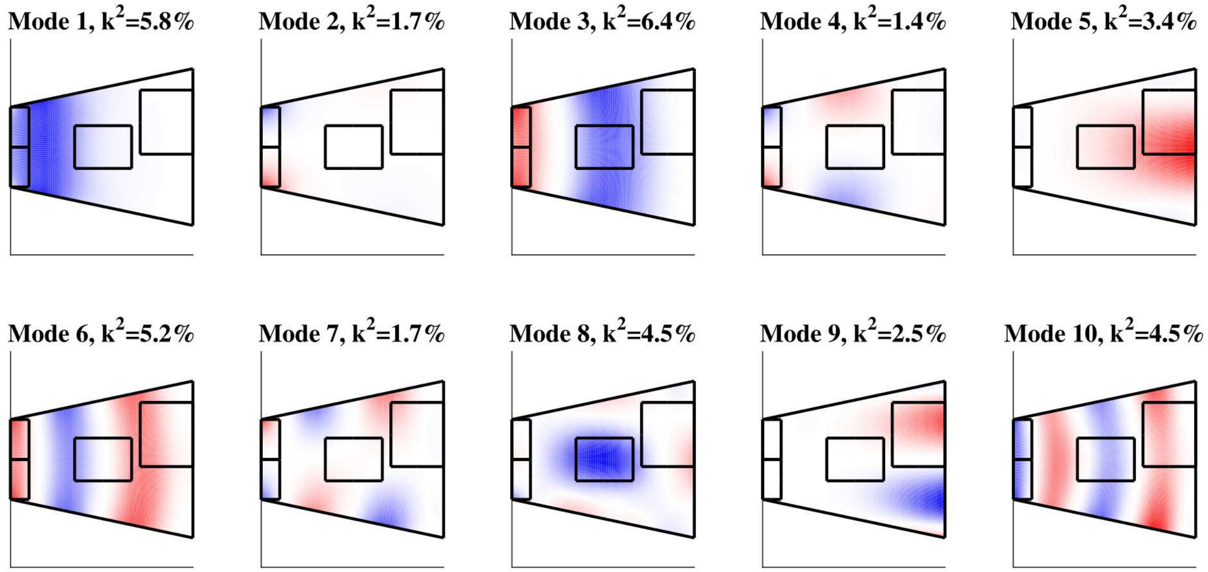

Fig. 7. Four piezoelectric patches enable good coupling for the first ten modes of the blade (colors show normalized signed strain energy)

canceled and there is no electrical energy available for vibration reduction. In contrast, placing the same piezoelectric patch volume in a region of high signed strain energy for both modes results in good coupling for both modes. Note that Figs. 4 and 6 show the signed strain energy for the plate without piezoelectric material since they display multiple iterations of patch locations; the stiffness of the patch typically only slightly alters the signed strain energy distribution.

In addition to location, the thickness of the piezoelectric patch affects the mechanical impedance of the patch, and therefore the strain transfer to the patch. Figure 5 illustrates the effect of changing the thickness for vibration reduction in modes 3 and 8; the location is fixed at a location of high signed strain energy for both modes. Each mode has a different optimal thickness for maximizing coupling, implying the need to find a compromise between the two optimal thicknesses to achieve good coupling in both modes. However, there is a relatively low loss in coupling near the optimal thicknesses. Note that the experimental setup had a volume ratio and thickness ratio of 1.9% and 13%, respectively. Thus, thicker piezoelectric patches could enable significant increases in coupling. However, size restrictions of the piezoelectric material for the turbomachinery environment may restrict the thickness to below the optimal value. Still, Fig. 5 and the experimental blade show that good coupling ($\sim k^2 > 1\%$) is attainable at very low thickness ratios.

Next, Fig. 6 illustrates optimization of piezoelectric patch location and size targeting vibration reduction in modes 5, 9, and 10 using the cost function in Eqn. (17). The piezoelectric material volume constraint is 5% of the volume of the plate. The optimized location for the piezoelectric material includes regions of high signed strain energy for all of the targeted modes and the optimal thickness is 31% the thickness of the plate. Figure 6 also includes the optimized topology for each mode without consideration of the other modes (e.g., $c_9 = c_{10} = 0$ for the fifth mode dotted patch). The individual-mode optimization produces thicker patches: thickness ratios are 98%, 45%, and 47% for modes 5, 9, and

10, respectively. Thus, simultaneous optimization of multiple modes sacrifices thickness to cover signed strain energy for all of the targeted modes. Note that while individual-mode optimization produces higher coupling for that mode, it leaves at least one of the other targeted modes with very poor coupling. For example, the high thickness ratio for the individual optimization of mode 5 shifts the strain energy of mode 10 away from the piezoelectric patch, resulting in nearly zero coupling in mode 10 (recall, the figures display the signed strain energy for the plate without piezoelectric material). However, high patch thicknesses are unrealistic for implementation anyway, further supporting the use of thin patches for multiple-mode vibration reduction.

5.2 Wideband Vibration Reduction

The previous examples show that placing piezoelectric material in regions of high signed strain energy for multiple modes enables good electromechanical coupling in those modes. However, it is not possible to target all vibration modes with a single piezoelectric patch due to the distribution of signed strain energy in the blade. For example, Fig. 7 shows that the signed strain energy for modes 1 and 5 are on opposite ends of the blade; a piezoelectric patch would have to span the entire blade length to have appreciable coupling in both modes. Optimization with multiple patches is difficult due to the additional constraints to prevent patch overlap and the dependence on the initial conditions. However, single-patch optimization provides insight into cases where optimization is difficult or costly: the signed strain energy distribution alone provides a tool for location selection while patch thickness and volume are limited by turbomachinery constraints. The signed strain energy distribution of the targeted modes drives the minimum number of patches required to achieve appreciable coupling in those modes.

To demonstrate the ability to achieve significant coupling across a wide range of modes, Fig. 7 presents a setup that uses four piezoelectric patches to reduce vibration across the first ten blade modes. The patch geometries and locations were manually selected based on the signed strain energy distribution in the ten modes with total volume limit of 5% the volume of the plate. The two patches at the root have thickness ratios $h_p/h = 0.25$ and the other two patches have $h_p/h = 0.12$. Each piezoelectric patch covers regions of signed strain energy for multiple modes; some modes have up to four patches contributing to their coupling. The root patches demonstrate the importance of the signed strain energy: torsional modes require a split root patch due to opposite signed strain energy at each edge, but bending modes benefit from root patches regardless of whether they are split. This configuration results in higher coupling than with a single patch for many of the modes while achieving sufficient coupling for more than twice the number of modes as number of piezoelectric patches.

Consider the application of RFD to the blade setup in Fig. 7. Assume the limiting case of zero sweep rate and a damping ratio of 0.1% for all modes. The torsional modes have the lowest coupling, ranging from 1.4% to 1.7%, which corresponds to maximum vibration amplitudes that are reduced by 73% and 77% from the baseline case. Chordwise-bending modes have coupling between 2.5% and 4.5%, resulting in vibration reduction of 84% and 91% of the open-circuit amplitudes, respectively. Finally, spanwise-bending coupling values range from 4.5% to 6.4%, producing a vibration reduction as high as 94% of the open-circuit amplitude. While physical implementations will experience decreased performance compared to this limiting case, these results demonstrate the potential to achieve vibration reduction in a relatively high number of modes with a relatively small amount of piezoelectric material.

6 Conclusions

This work develops a low-cost model to predict the electromechancial coupling of low-order representative turbomachinery blades, enabling optimization of piezoelectric material location and size. Tuning of optimization weights in the cost function enables prioritization of certain modes or compensation for modes that dominate the cost function. The signed strain energy is a significant factor in optimizing piezoelectric material location: the optimal location has relatively high signed strain energy in all of the targeted modes. This fact can be used for location optimization with more complicated geometries where analytical approximations are not possible. Strain energy predictions via finite element analysis of the blade alone may be used to find areas of high signed strain energy for all of the targeted modes as a starting point for design.

Finally, this paper demonstrates the potential to achieve significant vibration reduction across a wide range of modes with a relatively low number of piezoelectric patches that only occupy a small volume of the blade. Strategically placing piezoelectric patches in regions that cover signed strain energy for many modes results in large coupling due to the combined effects of each patch. While surface-mounted patches are not suitable for real turbomachinery blades, further investigation using embedded piezoelectric material may lead to suitable implementations (e.g., piezoelectric-coated fibers in composite blades).

Acknowledgements

The authors gratefully acknowledge support from the Office of Naval Research under grant number N00014-17-1-2527, monitored by Dr. Knox Millsaps and Dr. Steven Martens. The views and conclusions contained herein are those of the authors and should not be interpreted as necessarily representing the official policies or endorsements, either expressed or implied, of the Office of Naval Research, the U. S. Navy, or the U. S. government.

References

[1] EL-Aini, Y., deLaneuville, R., Stoner, A., and Capece, V., 1997. "High cycle fatigue of turbomachinery

components—industry perspective". In Proc. AIAA, AIAA, pp. 97–3365.

[2] Yu, H., and Wang, K. W., 2007. "Piezoelectric networks for vibration suppression of mistuned bladed disks". *J. Vib. Acoust.,* **129**(5), pp. 559–566.

[3] Yu, H., and Wang, K. W., 2009. "Vibration suppression of mistuned coupled-blade-disk systems using piezoelectric circuitry network". *J. Vib. Acoust.,* **131**(2), p. 021008.

[4] Kauffman, J. L., and Lesieutre, G. A., 2012. "Piezoelectric-based vibration reduction of turbomachinery bladed disks via resonance frequency detuning". *AIAA J.,* **50**(5), pp. 1137–1144.

[5] Lopp, G. K., and Kauffman, J. L., 2016. "Switch triggers for optimal vibration reduction via resonance frequency detuning". *J. Vib. Acoust.,* **138**(1), p. 011002.

[6] Lopp, G. K., and Kauffman, J. L., 2018. "Vibration reduction of mistuned bladed disks via piezoelectric-based resonance frequency detuning". *J. Vib. Acoust.,* **140**(5), p. 051007.

[7] Lopp, G. K., Kelley, C. R., and Kauffman, J. L., 2019. "Effect of turbomachinery blade root flexibility on electromechanical coupling for piezoelectric-based vibration reduction". In Proc. AIAA Scitech, AIAA.

[8] Kelley, C. R., and Kauffman, J. L., 2019. "Piezoelectric-based vibration reduction on pretwisted blades with centrifugal loads". In Proc. AIAA Scitech, AIAA.

[9] Duffy, K. P., Choi, B. B., Provenza, A. J., Min, J. B., and Kray, N., 2013. "Active piezoelectric vibration control of subscale composite fan blade". *J. Eng. Gas Turb. Power,* **135**(1), p. 011601.

[10] Min, J. B., Duffy, K. P., Choi, B. B., Provenza, A. J., and Kray, N., 2013. "Numerical modeling methodology and experimental study for piezoelectric vibration damping control of rotating composite fan blades". *Comput. Struct.,* **128**, pp. 230–242.

[11] Bachmann, F., de Oliveira, R., Sigg, A., Schnyder, V., Delpero, T., Jaehne, R., Bergamini, A., Michaud, V., and Ermanni, P., 2012. "Passive damping of composite blades using embedded piezoelectric modules or shape memory alloy wires: a comparative study". *Smart Mater. Struct.,* **21**(7), p. 075027.

[12] Wischt, R. J., and Garafolo, N., 2015. "Variable stiffness technique for turbomachinery using shape memory alloys". In Proceedings of AIAA Scitech 2015, AIAA.

[13] Wischt, R. J., and Garafolo, N., 2016. "The development of an active damping and stiffness technique for turbomachinery using shape memory alloys". In Proc. AIAA Scitech, AIAA.

[14] Bachmann, F., Bergamini, A. E., and Ermanni, P., 2012. "Optimum piezoelectric patch positioning: A strain energy-based finite element approach". *J. Intell. Mater. Syst. Struct.,* **23**(14), pp. 1575–1591.

[15] Ducarne, J., Thomas, O., and Deü, J., 2012. "Placement and dimension optimization of shunted piezoelectric patches for vibration reduction". *J. Sound Vib.,* **331**(14), pp. 3286–3303.

[16] Institute of Electrical and Electronics Engineers, 1987. IEEE Standard on Piezoelectricity. ANSI/IEEE Std. 176-1987, IEEE, New York, NY.

[17] Hagood, N. W., and von Flotow, A., 1991. "Damping of structural vibrations with piezoelectric materials and passive electrical networks". *J. Sound Vib.,* **146**(2), pp. 243–268.

[18] Hollkamp, J. J., 1994. "Multimodal passive vibration suppression with piezoelectric materials and resonant shunts". *J. Intell. Mater. Syst. Struct.,* **5**(1), pp. 49–57.

[19] Wu, S.-Y., 1998. "Method for multiple-mode shunt damping of structural vibration using a single pzt transducer". In Proc. SPIE, Vol. 3327, SPIE, pp. 159–168.

[20] Behrens, S., and Moheimani, S. O. R., 2002. "Current flowing multiple mode piezoelectric shunt dampener". In Proc. SPIE, Vol. 4697, SPIE, pp. 217–226.

[21] Toftekær, J. F., and Høgsberg, J., 2020. "Multi-mode piezoelectric shunt damping with residual mode correction by evaluation of modal charge and voltage". *J. Intell. Mater. Syst. Struct.,* **31**(4), pp. 570–586.

[22] Vasques, C. M. A., and Rodrigues, J. D., 2006. "Active vibration control of smart piezoelectric beams: Comparison of classical and optimal feedback control strategies". *Comput. Struct.,* **84**(22-23), pp. 1402–1414.

[23] Aridogan, U., and Basdogan, I., 2015. "A review of active vibration and noise suppression of plate-like structures with piezoelectric transducers". *J. Intell. Mater. Syst. Struct.,* **26**(12), pp. 1455–1476.

[24] Clark, W. W., 2000. "Vibration control with state-switched piezoelectric materials". *J. Intell. Mater. Syst. Struct.,* **11**(4), pp. 263–271.

[25] Richard, C., Guyomar, D., Audigier, D., and Ching, G., 1999. "Semi-passive damping using continuous switching of a piezoelectric device". In Proc. SPIE, Vol. 3672, SPIE, pp. 104–111.

[26] Richard, C., Guyomar, D., Audigier, D., and Bassaler, H., 2000. "Enhanced semi-passive damping using continuous switching of a piezoelectric device on an inductor". In Proc. SPIE, Vol. 3989, SPIE, pp. 288–299.

[27] Hynds, T. D., and Kauffman, J. L., 2015. "Harvesting at the margins: A study of energy harvesting away from optimal conditions". In Proceedings of AIAA Scitech 2015, AIAA.

[28] Kelley, C. R., and Kauffman, J. L., 2017. "Optimal switch timing for piezoelectric-based semi-active vibration reduction techniques". *J. Intell. Mater. Syst. Struct.,* **28**(16), pp. 2275–2285.

[29] Sadri, A. M., Wright, J. R., and Wynne, R. J., 1999. "Modelling and optimal placement of piezoelectric actuators in isotropic plates using genetic algorithms". *Smart Mater. Struct.,* **8**(4), pp. 490–498.

[30] Halim, D., and Moheimani, S. O. R., 2003. "An optimization approach to optimal placement of collocated piezoelectric actuators and sensors on a thin plate". *Mechatronics,* **13**(1), pp. 27–47.

[31] Peng, F., Ng, A., and Hu, Y.-R., 2005. "Actuator placement optimization and adaptive vibration control

of plate smart structures". *J. Intell. Mater. Syst. Struct.,* **16**(3), pp. 263–271.

[32] cheng Qiu, Z., min Zhang, X., xin Wu, H., and hua Zhang, H., 2007. "Optimal placement and active vibration control for piezoelectric smart flexible cantilever plate". *J. Sound Vib.,* **301**(3-5), pp. 521–543.

[33] Gupta, V., Sharma, M., and Thakur, N., 2010. "Optimization criteria for optimal placement of piezoelectric sensors and actuators on a smart structure: a technical review". *J. Intell. Mater. Syst. Struct.,* **21**(12), pp. 1227–1243.

[34] Kelley, C. R., and Kauffman, J. L., 2018. "Optimal placement and sizing of piezoelectric material for multiple-mode vibration reduction". In Proc. ASME Turbo Expo, Vol. GT2018-77025, ASME.

[35] Erturk, A., and Inman, D. J., 2011. *Piezoelectric Energy Harvesting*. John Wiley & Sons, Hoboken, NJ.

[36] Ewins, D. J., 2000. *Modal Testing: Theory, Practice, and Application*. John Wiley & Sons, Letchworth, England.

[37] Kauffman, J. L., 2012. "Vibration Reduction of Integrally Bladed Rotors Using Piezoelectric Materials". PhD thesis, Pennsylvania State University, December.

[38] Preumont, A., 2006. *Mechatronics*. Springer, Netherlands.

Appendix A: Assumed Modes Energy Formulation

The assumed modes method approximates the transverse displacement w as a summation of assumed shapes weighted by generalized coordinates q_{rs} [37]:

$$w(x,y,t) = \sum_{r=1}^{R}\sum_{s=1}^{S} q_{rs}(t)\varphi_{X,r}(x)\varphi_{Y,s}(y) \tag{19}$$

For this study, the assumed shapes in the x- and y- directions are:

$$\varphi_{X,r}(x) = \left(\frac{x}{a}\right)^{r+1} \tag{20}$$

$$\varphi_{Y,s}(x) = \left(\frac{y}{b_2}\right)^{s-1} \tag{21}$$

The model includes R shapes in the x-direction and S shapes in the y-direction. These assumed shapes in each direction form M combined assumed shapes for the entire plate:

$$\varphi_m(x,y) = \varphi_{X,r}(x)\varphi_{Y,s}(y) \tag{22}$$

$$m = (r-1)S + s \tag{23}$$

$$w(x,y,t) = \sum_{m=1}^{M} q_m(t)\varphi_m(x,y) \tag{24}$$

Although other assumed shapes might provide better convergence, these shapes offer the capability of performing analytical integration [37]. An analytical solution results in much faster computation, which is crucial for rapid prediction of coupling for optimization.

Each piezoelectric patch also requires analysis of the electrical state. The assumed shape for the voltage V_p of each patch is a linear variation through the thickness of the patch with generalized electrical coordinate q_{ep}:

$$V_p(z,t) = q_{ep}\frac{z-h/2}{h_p} \tag{25}$$

Strain Energy

The assumed modes method derives mass and stiffness matrices from energy terms. To start, the strain energy U_{strain} is the integral over the volume of the stress tensor σ_{ij} multiplied by the strain tensor ε_{ij}:

$$U_{\text{strain}} = \frac{1}{2}\int_V \sigma_{ij}\varepsilon_{ij}\mathrm{d}V \tag{26}$$

Stress-strain relations allow stress to be written in terms of strain and material constants:

$$\sigma_{xx} = \frac{E}{1-\nu^2}\varepsilon_{xx} + \frac{E\nu}{1-\nu^2}\varepsilon_{yy} \tag{27}$$

$$\sigma_{yy} = \frac{E\nu}{1-\nu^2}\varepsilon_{xx} + \frac{E}{1-\nu^2}\varepsilon_{yy} \tag{28}$$

$$\sigma_{xy} = \frac{E}{1+\nu}\varepsilon_{xy} \tag{29}$$

Classical plate theory provides the strain-displacement relations:

$$\varepsilon_{xx} = \varepsilon_{xx}^0 - z\frac{\partial^2 w}{\partial x^2} \tag{30}$$

$$\varepsilon_{yy} = \varepsilon_{yy}^0 - z\frac{\partial^2 w}{\partial y^2} \tag{31}$$

$$\varepsilon_{xy} = \varepsilon_{xy}^0 - z\frac{\partial^2 w}{\partial x\partial y} \tag{32}$$

Here, ε_{xx}^0, ε_{yy}^0, and ε_{xy}^0 refer to the midplane strains. Without any piezoelectric material, the plate is symmetric about the midplane and there is no bending-extension coupling. In practice, the piezoelectric material volume should be much smaller than the plate volume; therefore, assume any bending-extension coupling from the piezoelectric material is negligible. Thus, the midplane strains are zero for pure bending ($\varepsilon_{xx}^0 = \varepsilon_{yy}^0 = \varepsilon_{xy}^0 = 0$).

The stress-strain and strain-displacement relations along with the assumed displacement allow the strain energy to be written in terms of the generalized coordinates and derivatives of the assumed shapes. In fact, the strain energy may be written in the form:

$$U_{\text{strain}} = \frac{1}{2}\{q\}^t[K]\{q\} \tag{33}$$

Here, $\{q\}$ is a vector of the mechanical generalized coordinates and $[K]$ is a matrix with elements calculated by integrating over the volume of the blade:

$$
\begin{aligned}
[K]_{rsuv} = &\int_{\mathcal{V}} \frac{Ez^2}{1-\nu^2} \\
&\times \left[\frac{r(r+1)u(u+1)}{a^4} \left(\frac{x}{a}\right)^{r+u-2} \left(\frac{y}{b_2}\right)^{s+v-2} \right. \\
&+ \frac{(s-1)(s-2)(v-1)(v-2)}{b_2^4} \left(\frac{x}{a}\right)^{r+u+2} \left(\frac{y}{b_2}\right)^{s+v-6} \\
&+ \nu \frac{r(r+1)(v-1)(v-2)}{a^2 b_2^2} \left(\frac{x}{a}\right)^{r+u} \left(\frac{y}{b_2}\right)^{s+v-4} \\
&+ \nu \frac{u(u+1)(s-1)(s-2)}{a^2 b_2^2} \left(\frac{x}{a}\right)^{r+u} \left(\frac{y}{b_2}\right)^{s+v-4} \\
&+ 2(1-\nu) \frac{(r+1)(u+1)(s-1)(v-1)}{a^2 b_2^2} \\
&\left. \times \left(\frac{x}{a}\right)^{r+u} \left(\frac{y}{b_2}\right)^{s+v-4} \right] \mathrm{d}\mathcal{V}
\end{aligned}
\tag{34}
$$

Equation (34) calculates the m^{th} row and n^{th} column of the $[K]$ matrix, where Eqn. (23) relates r and s to m and, in an analogous fashion, u and v to n. The volume integral for the $[K]$ matrix is more tractable when broken into the volume integrals over the plate volume $\mathcal{V}_o$ and piezoelectric material volume $\mathcal{V}_p$:

$$
\int_{\mathcal{V}_o} d\mathcal{V}_o = \int_0^a \int_{-b(x)}^{b(x)} \int_{-h/2}^{h/2} \mathrm{d}z\, \mathrm{d}y\, \mathrm{d}x \tag{35}
$$

$$
\int_{\mathcal{V}_p} d\mathcal{V}_p = \sum_{p=1}^{P} \int_{x_{1p}}^{x_{2p}} \int_{y_{1p}}^{y_{2p}} \int_{h/2}^{h/2+h_p} \mathrm{d}z\, \mathrm{d}y\, \mathrm{d}x \tag{36}
$$

Integrating over the plate volume produces Eqn. (2) with the integral terms:

$$
I_1 = \begin{cases} C_1 \int_0^a x^{r+u-2} (b_1 + \frac{b_2-b_1}{a} x)^{s+v-1} \mathrm{d}x & \text{for } s+v \text{ even} \\ 0 & \text{for } s+v \text{ odd} \end{cases} \tag{37}
$$

$$
I_2 = \begin{cases} C_2 \int_0^a x^{r+u+2} (b_1 + \frac{b_2-b_1}{a} x)^{s+v-5} \mathrm{d}x & \text{for } s+v \text{ even; } s,v>2 \\ 0 & \text{for } s+v \text{ odd or } s \le 2 \text{ or } v \le 2 \end{cases} \tag{38}
$$

$$
I_3 = \begin{cases} C_3 \int_0^a x^{r+u} (b_1 + \frac{b_2-b_1}{a} x)^{s+v-3} \mathrm{d}x & \text{for } s+v \text{ even; } v>2 \\ 0 & \text{for } s+v \text{ odd or } v \le 2 \end{cases} \tag{39}
$$

$$
I_4 = \begin{cases} C_4 \int_0^a x^{r+u} (b_1 + \frac{b_2-b_1}{a} x)^{s+v-3} \mathrm{d}x & \text{for } s+v \text{ even; } s>2 \\ 0 & \text{for } s+v \text{ odd or } s \le 2 \end{cases} \tag{40}
$$

$$
I_5 = \begin{cases} C_5 \int_0^a x^{r+u} (b_1 + \frac{b_2-b_1}{a} x)^{s+v-3} \mathrm{d}x & \text{for } s+v \text{ even; } s,v>1 \\ 0 & \text{for } s+v \text{ odd or } s=1 \text{ or } v=1 \end{cases} \tag{41}
$$

$$
C_1 = \frac{2r(r+1)u(u+1)}{(s+v-1)a^{r+u+2} b_2^{s+v-2}} \tag{42}
$$

$$
C_2 = \frac{2(s-1)(s-2)(v-1)(v-2)}{(s+v-5)a^{r+u+2} b_2^{s+v-2}} \tag{43}
$$

$$
C_3 = 2\nu \frac{r(r+1)(v-1)(v-2)}{(s+v-3)a^{r+u+2} b_2^{s+v-2}} \tag{44}
$$

$$
C_4 = 2\nu \frac{u(u+1)(s-1)(s-2)}{(s+v-3)a^{r+u+2} b_2^{s+v-2}} \tag{45}
$$

$$
C_5 = 4(1-\nu) \frac{(r+1)(u+1)(s-1)(v-1)}{(s+v-3)a^{r+u+2} b_2^{s+v-2}} \tag{46}
$$

Integration over the piezoelectric material region produces Eqn. (4) with integral terms:

$$
I_{1p} = C_{1p} (x_{2p}^{r+u-1} - x_{1p}^{r+u-1})(y_{2p}^{s+v-1} - y_{1p}^{s+v-1}) \tag{47}
$$

$$
I_{2p} = C_{2p} (x_{2p}^{r+u+3} - x_{1p}^{r+u+3})(y_{2p}^{s+v-5} - y_{1p}^{s+v-5}) \tag{48}
$$

$$
I_{3p} = C_{3p} (x_{2p}^{r+u+1} - x_{1p}^{r+u+1})(y_{2p}^{s+v-3} - y_{1p}^{s+v-3}) \tag{49}
$$

$$
I_{4p} = C_{4p} (x_{2p}^{r+u+1} - x_{1p}^{r+u+1})(y_{2p}^{s+v-3} - y_{1p}^{s+v-3}) \tag{50}
$$

$$
I_{5p} = C_{5p} (x_{2p}^{r+u+1} - x_{1p}^{r+u+1})(y_{2p}^{s+v-3} - y_{1p}^{s+v-3}) \tag{51}
$$

These piezoelectric integrals do not depend on whether $s+v$ is even or odd since the piezoelectric material is not, necessarily, symmetric with respect to the coordinates. However, each integral is zero for the same s and v values corresponding to zero-valued derivatives as written explicitly for the plate integrals (e.g., $I_{3p} = 0$ for $v \le 2$). The constant coefficients in the piezoelectric integrals are equal to the corresponding coefficients for the plate divided by twice the power of x in each integral solution, while also replacing ν with ν_p (i.e., $C_{1p} = \frac{C_1}{2(r+u-1)}$, $C_{2p} = \frac{C_2}{2(r+u+3)}$, etc.).

Electrical and Coupled Energy

Analysis of the electrical energy and coupled energy captures the effect of the electromechanical coupling. The electrical energy U_{elec} is:

$$
U_{\text{elec}} = \sum_{p=1}^{P} \frac{1}{2} \int_{\mathcal{V}_p} \varepsilon_p \left(-\frac{\partial V_p}{\partial z} \right)^2 \mathrm{d}\mathcal{V}_p \tag{52}
$$

Here, ε_p is the dielectric constant of the piezoelectric material at a constant strain. Integrating over the volume of the piezoelectric material produces:

$$U_{\text{elec}} = \sum_{p=1}^{P} \frac{1}{2} q_{pe}^2 \frac{\varepsilon_p A_p}{h_p} \tag{53}$$

Here, A_p is the in-plane area of the p^{th} piezoelectric patch. Now the electrical potential energy may be written in the form:

$$U_{\text{elec}} = \frac{1}{2}\{q_e\}^t [K_e]\{q_e\} \tag{54}$$

Thus, the elements of the electrical stiffness matrix are in the form of Eqn. (6)

The piezoelectric material also results in a coupled energy U_{coupled} that includes the mechanical strain and the electrical potential [38]. While $U_{\text{coupled}} = 0$, it provides a mechanism to couple work and energy across domains. Most piezoelectric patches exhibit in-plane isotropy ($e_{31} = e_{32}$), so the coupled energy is:

$$\begin{aligned} U_{\text{coupled}} = & \sum_{p=1}^{P} \frac{1}{2} \int_{\forall_p} \left(-\frac{\partial V_p}{\partial z}\right) e_{31p}(\varepsilon_{xx} + \varepsilon_{yy}) \mathrm{d}\forall_p \\ & - \sum_{p=1}^{P} \frac{1}{2} \int_{\forall_p} e_{31p}(\varepsilon_{xx} + \varepsilon_{yy}) \left(-\frac{\partial V_p}{\partial z}\right) \mathrm{d}\forall_p \end{aligned} \tag{55}$$

Substituting for the strain and voltage produces:

$$U_{\text{coupled}} = \frac{1}{2}\{q_e\}^t [K_c]\{q_m\} - \frac{1}{2}\{q_m\}^t [K_c]^t \{q_e\} \tag{56}$$

Here, the coupled stiffness matrix elements are:

$$\begin{aligned} [K_c]_{prs} = & \sum_{p=1}^{P} \int_{\forall_p} e_{31p} \frac{z}{h_p} \left[\frac{r(r+1)}{a^2} \left(\frac{x}{a}\right)^{r-1} \left(\frac{y}{b_2}\right)^{s-1} \right. \\ & \left. + \frac{(s-1)(s-2)}{b_2^2} \left(\frac{x}{a}\right)^{r+1} \left(\frac{y}{b_2}\right)^{s-3} \right] \mathrm{d}\forall_p \end{aligned} \tag{57}$$

Integrating over the volume produces Eqn. (7).

Kinetic Energy

Finally, the kinetic energy T leads to the mass matrix for the representative blade:

$$T = \frac{1}{2} \int_{\forall} \rho \left(\frac{\partial w}{\partial t}\right)^2 \mathrm{d}\forall \tag{58}$$

The kinetic energy may be rewritten to define the mass matrix $[M]$:

$$T = \frac{1}{2}\{\dot{q}\}^t [M]\{\dot{q}\} \tag{59}$$

This form of the kinetic energy produces the integral for the mass matrix:

$$[M]_{rsuv} = \int_{\forall} \rho \left(\frac{x}{a}\right)^{r+u+2} \left(\frac{y}{b_2}\right)^{s+v-2} \mathrm{d}\forall \tag{60}$$

Integrating the mass matrix over the plate volume produces Eqn. (8).

Rotated Piezoelectric Patches

The previously calculated system matrices correspond to piezoelectric patches with zero rotation about the z-axis. Inclusion of rotated piezoelectric patches requires a change in coordinates to calculate piezoelectric contributions to the system matrices. The coordinate transformation from the xy- to $\alpha\beta$-system via a counterclockwise rotation θ of the piezoelectric patch about its centroid is:

$$\begin{Bmatrix} x \\ y \end{Bmatrix} = \begin{bmatrix} \cos\theta & -\sin\theta \\ \sin\theta & \cos\theta \end{bmatrix} \begin{Bmatrix} \alpha \\ \beta \end{Bmatrix} \tag{61}$$

Looking back at the previous analysis, all of the integrals are of the form:

$$I = \int\int x^{n_x} y^{n_y}\, \mathrm{d}y\, \mathrm{d}x \tag{62}$$

Using the coordinate transformation, this integral becomes:

$$I = \int_{\alpha_-}^{\alpha_+} \int_{\beta_-}^{\beta_+} (\alpha\cos\theta - \beta\sin\theta)^{n_x} (\alpha\sin\theta + \beta\cos\theta)^{n_y}\, \mathrm{d}\beta\, \mathrm{d}\alpha \tag{63}$$

Here, α_-, α_+, β_-, and β_+ are the bounds of the piezoelectric patch in the $\alpha\beta$-system, which may be calculated from the bounds in the xy-system by applying the coordinate transformation in Eqn. (61). Applying the binomial theorem allows the integral to be solved analytically:

$$\begin{aligned} I = & \sum_{i=0}^{n_x} \sum_{j=0}^{n_y} C_{ij} (\alpha_+^{n_x+n_y-i-j+1} - \alpha_-^{n_x+n_y-i-j+1}) \\ & \times (\beta_+^{i+j+1} - \beta_-^{i+j+1}) \end{aligned} \tag{64}$$

$$C_{ij} = \frac{n_x! n_y! (-1)^i (\sin\theta)^{n_y+i-j} (\cos\theta)^{n_x-i+j}}{i! j! (n_x-i)! (n_y-j)! (n_x+n_y-i+j+1)(i+j+1)} \tag{65}$$